

# Monte Carlo approach for solving the radiative transfer equation over mountainous and heterogeneous areas

Christophe Miesch, Xavier Briottet, Yann H. Kerr, and François Cabot

An algorithm based on the Monte Carlo method is developed to solve the radiative transfer equation in the reflective domain (0.4–4  $\mu\text{m}$ ) of the solar spectrum over rugged terrain. This algorithm takes into account relief, spatial heterogeneity, and ground bidirectional reflectance. The method permits the computation of irradiance components at ground level and radiance terms reaching an airborne or satelliteborne sensor. The Monte Carlo method consists of statistically simulating the paths of photons inside the Earth–atmosphere system to reproduce physical phenomena while introducing neither analytical modeling nor assumption. The potentialities of the code are then depicted over different types of landscape, including a seashore, a desert region, and a steep mountainous valley. © 1999 Optical Society of America

OCIS codes: 010.1300, 280.0280, 000.5490.

## 1. Introduction

Remotely sensed data measured in the solar reflective domain (0.4–4  $\mu\text{m}$ ) are often used for the assessment of the spatial distribution of surface properties. In analyses of such data for mountainous or heterogeneous areas, the assumptions that are valid for flat and homogeneous terrains no longer produce accurate results, and appropriate corrections to the radiative transfer model need to be made. In the case of a rugged and heterogeneous scene, the orientation of an observed pixel with respect to the Sun and the sensor, together with its radiometric properties, can be significantly different from that of its neighbors. These properties directly affect the irradiance that reaches a pixel at ground level and subsequently the radiance field produced toward the sensor. Moreover, the topography introduces new contributions from neighboring pixels to the ground irradiance.

To model accurately the radiative signal received at aircraft or satellite level, one must take into account the spatial variability of the ground surface.

Several authors have presented different models to simulate solar irradiance on rugged terrains and have proposed various correction methods. Most of these models perform a cosine correction of the local zenith angle of the direct incident beam<sup>1</sup>; they also take into account shadowing introduced by topography. Kimes and Kirchner<sup>2</sup> developed a model of irradiance at ground level that also considers the anisotropy of the diffuse sky irradiance and the reflections from adjacent slopes. Using this advanced model, they demonstrated that the use of simple models that take into account only direct solar irradiance can introduce significant errors. For example, an 11% or greater error in reflectance (at ground level) occurs over a vegetation canopy in a red band when surface slopes exceed 20°. Kusaka *et al.*<sup>3–5</sup> analyzed the effects of topographic and atmospheric effects to account for them in satellite data. Their model is applicable over a Lambertian heterogeneous landscape and integrates slope and shading effects on direct irradiance and on diffuse sky irradiance. However, they neglected the effect of surrounding pixels. Richter,<sup>6</sup> who presented an overview of studies on the subject, also used an atmospheric and topographic correction model for high-resolution sensor data. Assuming a Lambertian surface, he considered a model that includes direct irradiance coupled with isotropic sky radiance. He computed an approximate correction for adjacency effects (reflections

---

C. Miesch (christophe.miesch@oncert.fr) and X. Briottet (xavier.briottet@oncert.fr) are with the Département d'Optique Théorique et Appliquée, Office National d'Etudes et de Recherches Aéropatiales, 2 avenue E. Belin, 31400 Toulouse, France. Y. H. Kerr (yann.kerr@cesbio.cnes.fr) is with the Centre d'Etudes Spatiales de la Biosphère, 18 avenue E. Belin, 31400 Toulouse, France. F. Cabot (francois.cabot@cst.cnes.fr) is with the Centre National d'Etudes Spatiales, Qualité et Traitements des Images Satellitaires, 18 avenue E. Belin, 31400 Toulouse, France.

Received 8 February 1999; revised manuscript received 8 September 1999.

0003-6935/99/367419-12\$15.00/0

© 1999 Optical Society of America

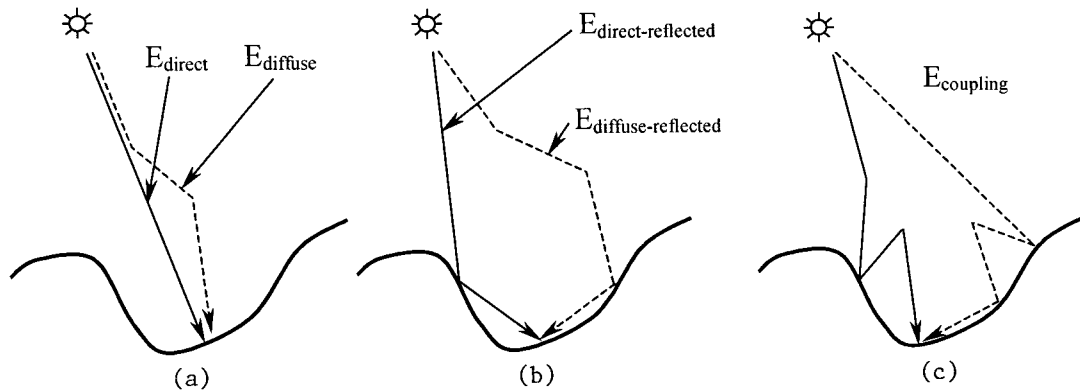


Fig. 1. Irradiance components at ground level.

on neighboring pixels) on sensor radiance, using an average reflectance of neighboring pixels, but, similarly to Kusaka *et al.*,<sup>3,4,5</sup> he did not consider the adjacency and Earth-atmosphere coupling terms at ground level. He reckoned that the corresponding error becomes significant for deep valleys or highly reflecting surfaces. Proy *et al.*,<sup>7</sup> who developed a model to evaluate ground irradiance over mountainous terrain, introduced an Earth-atmosphere coupling term (multiple reflections between ground and atmosphere), but its role was considered negligible and was not taken into account. Vermote *et al.*<sup>8</sup> developed a radiative transfer code (6S) adapted to flat surfaces. Few assumptions were made over homogeneous ground. However, for a target surrounded by an environment of a different nature, the environment contribution function introduced in the computation of the Earth-atmosphere coupling irradiance term is subject to simplifying approximations. Moreover, this code cannot deal with more-complex ground heterogeneity.

Our goal in this paper is to evaluate the radiance observed by a sensor over a mountainous area to quantify the various contributions to the measured radiance. In particular, the contributions that come from, or are altered by, topography or the spatial heterogeneity of the ground surface are investigated in detail. To this end we developed a radiative transfer model based on the Monte Carlo principle<sup>9</sup> and applied the model to diverse surface types, including mountainous regions and heterogeneous areas. To check the validity of the Monte Carlo approach, we shall compare some results with those obtained with the 6S code<sup>8</sup> for flat and homogeneous terrain.

## 2. Monte Carlo Method

### A. Physical Model

The signal emitted by the Sun and received by the sensor can travel on different paths. Let us consider first the Sun-to-surface path illustrated in Fig. 1. Three main types of interaction can be identified. The most obvious interactions are those of direct and diffuse paths [Fig. 1(a)]. Over rugged terrain a pho-

ton may be reflected by neighboring pixels before it reaches the target [Fig. 1(b)]. These photons contribute to what we call the adjacency component. Finally, the Earth-atmosphere coupling irradiance term describes photons that have been subject to multiple surface reflections and atmospheric scatterings [Fig. 1(c)]. This term is also called the environmental component.

Most of the photons in an Earth-to-sensor path come directly from the target [Fig. 2(a)]. However, photons at the sensor can also correspond to scattered photons coming either from the target or from neighboring pixels [Fig. 2(b)]. Finally, photons that were scattered in the atmosphere without reaching the surface can reach the sensor [Fig. 2(c)]. They correspond to the atmospheric intrinsic radiance.

### B. Main Principles of the Method

To compute the components of the radiative field, we compute the paths of photons inside the Earth-atmosphere system by the Monte Carlo principle.<sup>9</sup> The idea is to consider individual photons and to reproduce statistically the macroscopic effects in the system. First, a photon is characterized by its position and propagation direction. Three basic physical phenomena may then occur to this photon: absorption and scattering by particles (gaseous molecules and aerosols) and reflection by the ground. The path of a photon comes to an end when the photon is either absorbed or leaves the atmosphere. Its behavior in the system is governed by the statistical law that results directly from the equation of radiative transfer<sup>10</sup> (Appendix A).

### C. Specificities of the Code

The present Monte Carlo code assumes a plane-parallel and horizontally invariant atmosphere, so its properties depend only on altitude. Consequently, any variations in the aerosol content profile from one position to another over the scene are neglected. The atmosphere is divided into elementary homogeneous layers, and the extinction and scattering coefficients for both molecules and aerosols are computed at a specified monochromatic wavelength.

The scene is represented by a digital elevation

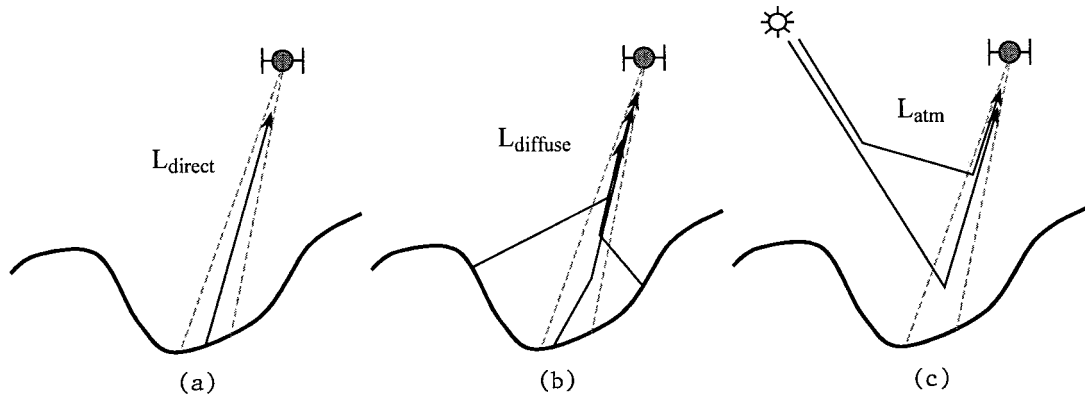


Fig. 2. Radiance components at sensor level.

model (DEM), the resolution of which is fixed by a horizontal regular grid. Each pixel of the DEM, which is completely described by the altitude of its center point and a unitary vector orthogonal to its surface, is associated with a spectral bidirectional reflectance model. Ground homogeneity is assumed within each pixel. The DEM is taken to be periodic at the boundaries of the model domain in both horizontal directions (Fig. 3).

#### D. Actual Algorithm

For a simulation made as described in Appendix A, the number of photons received by the sensor is small in relation to the number of launched photons. Consequently, it is more efficient to divide the simulation into three steps. The first step is devoted to the characterization of the downward path (from Sun to surface). This step allows one to assess the spatial distribution of the incident photons on each pixel at

ground level and the corresponding irradiance. The second step is to compute the upward path (from surface to sensor). This step is most easily performed by use of a reverse Monte Carlo method: The photons are launched from the sensor and counted at ground level. From Helmholtz's reciprocity principle, the resultant path characterization is equivalent to that obtained from the Monte Carlo method, but the process is much more efficient in terms of computation time. In this upward-path simulation process the reflection of photons from the surface is not accounted for, as it was already taken into account in the downward-path simulation. The last step consists of merging the two simulations, i.e., in connecting the two spatial distributions of incident photons at ground level (obtained by the first and second steps) through the use of the bidirectional reflectance.

The satellite signal results from the boundary conditions represented by the bidirectional reflectance at ground level. To write the radiance expression of a pixel  $m$  at sensor level, let us suppose that we launched  $N$  photons across the horizontal surface area  $S_{\text{TOA}}$  at the top of the atmosphere (TOA). Consider now that  $n_M(\Delta\omega_1)$  is the number of photons coming from the Sun and received by pixel  $M$  (of surface  $S_M$ ) at ground level in the elementary solid angle  $\Delta\omega_1$  (step 1) and that  $n_M'(m, \Delta\omega_2)$  is the number of photons launched from pixel  $m$  at sensor level and received by  $M$  in  $\Delta\omega_2$  (step 2). If  $\rho(\Delta\omega_1, \Delta\omega_2)$  is the bidirectional reflectance value associated with the incident direction  $\Delta\omega_1$  and the reflected direction  $\Delta\omega_2$ , the contribution of pixel  $M$  of the ground to the signal received by  $m$  is

$$\Delta L(m) = \sum_{\Delta\omega_1 \in \Omega} \sum_{\Delta\omega_2 \in \Omega} \left[ \frac{n_M(\Delta\omega_1)}{S_M} \right] \left[ \frac{\rho(\Delta\omega_1, \Delta\omega_2)}{\pi} \right] \times \left[ \frac{n_M'(m, \Delta\omega_2)}{N'} \right] \left( \frac{S_{\text{TOA}}}{N} E_{\text{TOA}} \cos \theta_s \right), \quad (1)$$

where  $N$  and  $N'$  are the number of photons launched from the Sun (i.e., the top of the atmosphere) and from  $m$  (i.e., the sensor), respectively, and  $E_{\text{TOA}} \cos(\theta_s)$  is the irradiance incident at the TOA. One can compute the direct and diffuse upward paths by

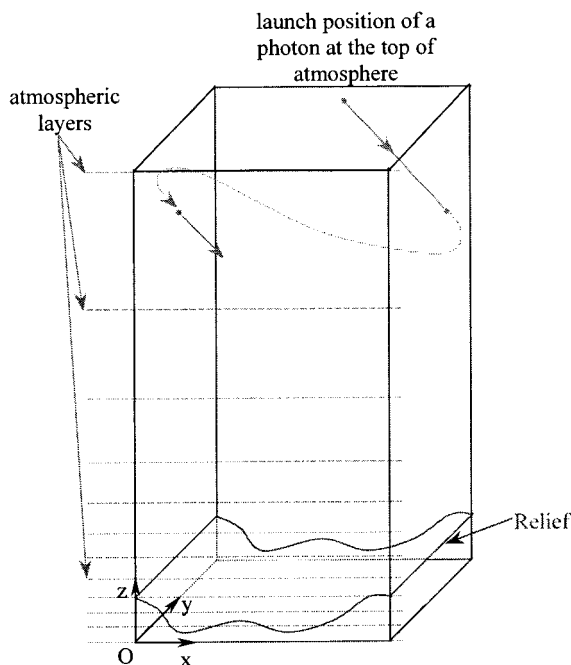


Fig. 3. Earth-atmosphere system.

**Table 1. Comparison of Monte Carlo and 6S Codes for  $\theta_s = 30^\circ$ ,  $\theta_v = 0^\circ$ , and  $v = 23$  km**

| Code and Relative Deviation <sup>a</sup> | Irradiance Components at Ground Level<br>(W m <sup>-2</sup> μm <sup>-1</sup> ) |                      |                       |                    | Radiance Components at Sensor Level<br>(W m <sup>-2</sup> μm <sup>-1</sup> sr <sup>-1</sup> ) |                      |                  |                    |
|--|--|----------------------|-----------------------|--------------------|---|----------------------|------------------|--------------------|
|  | $E_{\text{direct}}$  | $E_{\text{diffuse}}$ | $E_{\text{coupling}}$ | $E_{\text{total}}$ | $L_{\text{direct}}$   | $L_{\text{diffuse}}$ | $L_{\text{atm}}$ | $L_{\text{total}}$ |
| Monte Carlo code                         | 1099.5   | 355.7                | 60.6                  | 1515.8             | 100.5   | 28.1                 | 25.6             | 154.2              |
| 6S code                                  | 1099.3   | 363.6                | 58.3                  | 1521.2             | 100.8   | 28.8                 | 24.7             | 154.3              |
| Deviation $\delta$ (%)                   | <0.5   | -2.2                 | 3.9                   | <0.5               | <0.5  | -2.4                 | 3.6              | <0.5               |

<sup>a</sup>Relative deviation  $\delta$  is given by  $\delta = 100 \times (\text{MC} - \text{6S})/\text{6S}$ , where MC means Monte Carlo.

accumulating photons for each component separately during the upward simulation.

The atmospheric intrinsic radiance is determined by this upward simulation, too. The photons launched from the sensor that go out of the atmosphere are analyzed. If they did not reach the surface and if their direction is inside a solid angle  $\Delta\omega_s$  about the solar direction ( $\theta_s, \phi_s$ ), they contribute to the atmospheric radiance. If  $n_{\text{atm}}'(m, \Delta\omega_s)$  is the number of such photons, the atmospheric radiance expression is then

$$L_{\text{atm}}(m) = \frac{n_{\text{atm}}'(m, \Delta\omega_s) E_{\text{TOA}}}{N' \Delta\omega_s}. \quad (2)$$

The last term in Eq. (2) is the one that requires the most photon path simulations, as it is associated with an almost parallel beam, leading to a small solid angle  $\Delta\omega_s$ . The total radiance received on pixel  $m$  of the sensor is then obtained by

$$L(m) = L_{\text{atm}}(m) + \sum_{M \in \text{DEM}} \left\{ \sum_{\Delta\omega_1 \in \Omega} \sum_{\Delta\omega_2 \in \Omega} \left[ \frac{n_M(\Delta\omega_1)}{S_M} \right] \times \left[ \frac{\rho(\Delta\omega_1, \Delta\omega_2)}{\pi} \right] \left[ \frac{n_M'(m, \Delta\omega_2)}{N'} \right] \right\} \times \left( \frac{S}{N} E_{\text{TOA}} \cos \theta_s \right). \quad (3)$$

#### E. Comparison with Code 6S

To validate the Monte Carlo code, we compare its output with that of the 6S radiative transfer code. To fulfill the 6S operating conditions, the ground is necessarily flat and homogeneous. Its reflectance follows Lambert's law and is set to 0.3. The model of the atmosphere is the mid-altitude winter model of McClatchey *et al.*,<sup>11</sup> and we consider a wavelength of

550 nm. The aerosols are modeled by the Junge power law<sup>10</sup> with 23-km visibility. The solar zenith angle is arbitrarily chosen at  $30^\circ$ , while the satellite-borne sensor is nadir viewing. Results produced by the Monte Carlo and 6S codes for this case are presented in Table 1. The direct component at ground level is the simplest path to evaluate, so the difference in this quantity between the two methods is less than 0.5%. A more interesting comparison is the results for the diffuse components. It appears that the Monte Carlo method gives greater importance to backscattering than does the 6S code. This explains the facts that the Monte Carlo diffuse irradiance at ground level is lower and that the coupling term is higher.

We perform another test by using both a larger air mass (by setting the viewing zenith angle to  $30^\circ$ ) and a smaller aerosol visibility of 10 km. The sensor is placed in the principal (solar) plane opposite the Sun. The results, similar to those in Table 1, are presented in Table 2. Note that for the terms directly related to sky radiances, the differences are slightly more marked than in the previous case, as a result of the greater optical thickness of the atmosphere being viewed.

A comparison of the results obtained by the Monte Carlo method and the 6S code demonstrates the validity of the Monte Carlo code for flat landscapes. As the Monte Carlo method does not make any modeling assumptions, the slight difference noted between the two sets of results could be attributed to numerical approximations performed in the 6S method. This type of comparison, even though it is limited and approximate, is currently the only one that permits an assessment of the validity of the Monte Carlo code. Nevertheless, the Monte Carlo method developed in this study can reasonably be assumed to deliver re-

**Table 2. Comparison of Monte Carlo and 6S Codes for  $\theta_s = 30^\circ$ ,  $\theta_v = 30^\circ$ , and  $v = 10$  km<sup>a</sup>**

| Code and Relative Deviation <sup>a</sup> | Irradiance Components at Ground Level<br>(W m <sup>-2</sup> μm <sup>-1</sup> ) |                      |                       |                    | Radiance Components at Sensor Level<br>(W m <sup>-2</sup> μm <sup>-1</sup> sr <sup>-1</sup> ) |                      |                  |                    |
|--|--|----------------------|-----------------------|--------------------|---|----------------------|------------------|--------------------|
|  | $E_{\text{direct}}$  | $E_{\text{diffuse}}$ | $E_{\text{coupling}}$ | $E_{\text{total}}$ | $L_{\text{direct}}$   | $L_{\text{diffuse}}$ | $L_{\text{atm}}$ | $L_{\text{total}}$ |
| Monte Carlo                              | 875.6  | 518.3                | 73.6                  | 1467.5             | 73.2  | 43.3                 | 31.9             | 148.4              |
| 6S code                                  | 875.2  | 532.8                | 69.7                  | 1477.7             | 73.7  | 44.9                 | 29.7             | 148.3              |
| Deviation $\delta$ (%)                   | <0.5   | -2.7                 | 5.6                   | -0.7               | 0.7   | -3.6                 | 7.4              | <0.5               |

Relative deviation  $\delta$  is given by  $\delta = 100 \times (\text{MC} - \text{6S})/\text{6S}$ , where MC means Monte Carlo.

alistic physical results over rugged and heterogeneous landscapes.

### 3. Simulations

We apply the Monte Carlo method described above to various topographic and atmospheric configurations to illustrate its capabilities and the different effects that may be observed over these landscapes. As we previously explained, the scenes that are used in the Monte Carlo simulation have periodic boundary conditions along both horizontal axes. In the following cases, the scenes are defined by a relief profile that is invariant along the transversal axis ( $y$  axis in Fig. 3). Because the sensor is at satellite level (i.e., far from the scene), it can be considered that an observation is completely known if the signal that corresponds to an elementary profile is characterized. This property is not used during computation, but it helps in presenting the results.

#### A. Observation of a Reflectance Step at Ground Level

The first simulation is for a flat terrain composed of sand and water (e.g., open water next to a beach of sand). Such a configuration illustrates the effect of the atmosphere on the observation of a sharp boundary at ground level (Fig. 4). The ratio of the atmospheric depth to the length across the sand and water is sufficiently small to reduce the environmental effect introduced by the periodicity of the DEM. At a wavelength of 550 nm, reflectances are Lambertian, and their values are 0.35 for sand (medium sandstone<sup>12</sup>) and 0.03 for water (seawater<sup>12</sup>). The atmo-

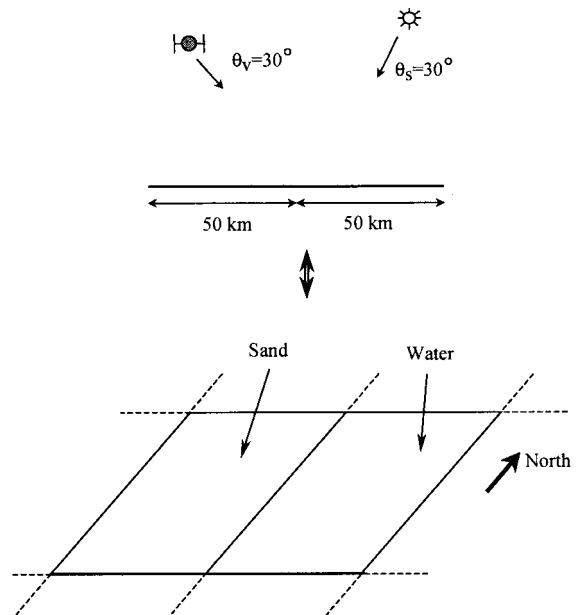


Fig. 4. Seashore landscape.

sphere is represented by a mid-latitude winter profile.<sup>11</sup> The aerosols are modeled by the Junge power law,<sup>10</sup> and their abundance is fixed by a horizontal visibility of 10 km. The Sun's zenith angle is set at 30° and its azimuth angle at 90°. The sensor is satelliteborne (800 km high) with a zenith angle of 30° and an azimuth angle of 270°.

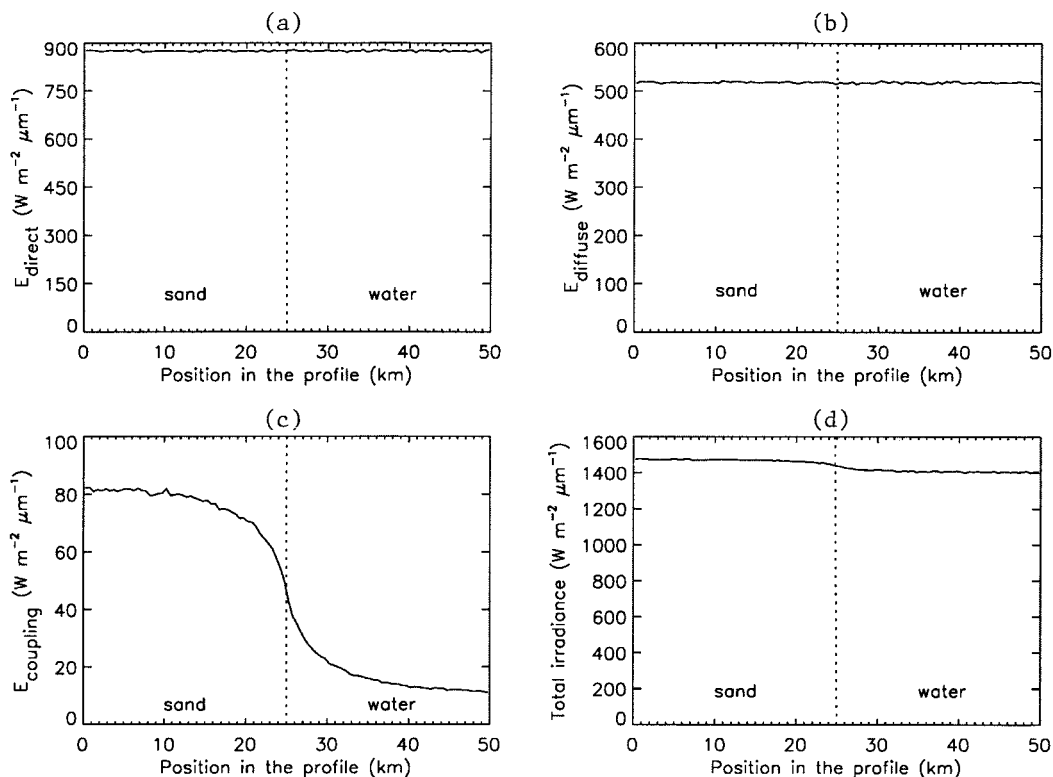


Fig. 5. Irradiance components at ground level on the seashore.

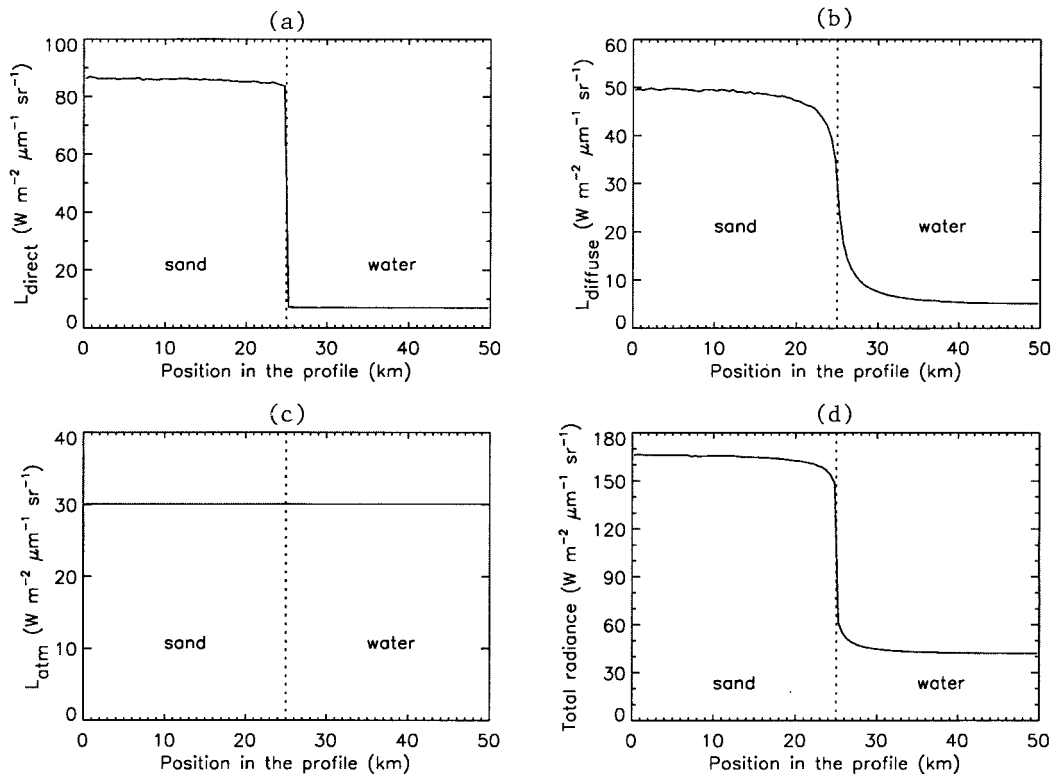


Fig. 6. Radiance components received by the sensor over the seashore.

The surface irradiance components computed by the Monte Carlo method are plotted as a function of the position (in kilometers) along the  $x$  axis (Fig. 5). The radiance components correspond to a pixel at sensor level, but as each pixel is associated with one and only one pixel at ground level (through the instrument instantaneous field of view) we use the same horizontal axis, graduated in kilometers, to plot the results (Fig. 6).

At ground level the direct and diffuse components are invariant over the entire flat terrain. The Earth-atmosphere coupling term is much more interesting because it is influenced by the neighboring pixels, and the relative importance of neighboring pixels decreases with the distance that separates them. The maximum and minimum values observed in Fig. 5(c) correspond to the signal that would have been obtained from a homogeneous sand scene and a homogeneous sea scene, respectively. The decrease of the signal from 0 to 50 km results from the variation of the environment reflectance, which is, on average, diminishing. This decrease is important in relation to the mean value of the coupling term (the difference between the signal and its mean value reaches  $\sim 70\%$  of this mean value), but neglecting it in this case would introduce less than a 6% error in the total irradiance at ground level.

Because the total irradiance term is only slightly variable, the direct upward radiance component presents a clear step that is associated with the sand-water boundary. The diffuse upward radiance is smoother over the boundary, behaving in a manner

similar to the coupling irradiance. The atmospheric intrinsic radiance is an additive signal that is identical for all sensor pixels, so it does not introduce any asymmetry into the total radiance. As the total radiance in Fig. 6(d) illustrates, on both sides of the boundary ( $\pm 2$  km) the error may amount to 5% if the sand-water boundary is neglected in the radiative transfer model. Such effects may have to be taken into account, especially in high resolution images. Another important point illustrated by this simulation is that one can use the Monte Carlo method to evaluate the atmospheric modulation transfer function.<sup>13</sup>

#### B. Adjacency and Environmental Effects on Linear Dunes

The goal of this simulation is to evaluate the relative contributions to surface irradiance of the adjacency and environmental terms at ground level over a poorly exposed area (the direct component is low) with a highly reflecting surface. The example we choose here is Saharian sand dunes<sup>14</sup> (Fig. 7). The linear dunes are entirely covered by sand and have a Lambertian reflectance of 0.4 at 550 nm. The atmospheric model is again the mid-latitude winter profile<sup>11</sup> with a 10-km aerosol visibility. The Sun's zenith angle is set to  $45^\circ$ , and the principal plane is orthogonal to a dune's direction. This configuration gives low illumination on one side of the dune, as a result of the low local incidence of the solar beam.

The resultant direct irradiance component [Fig. 8(a)] confirms the importance of the pixel orientation in relation to the incident direct solar beam. It also

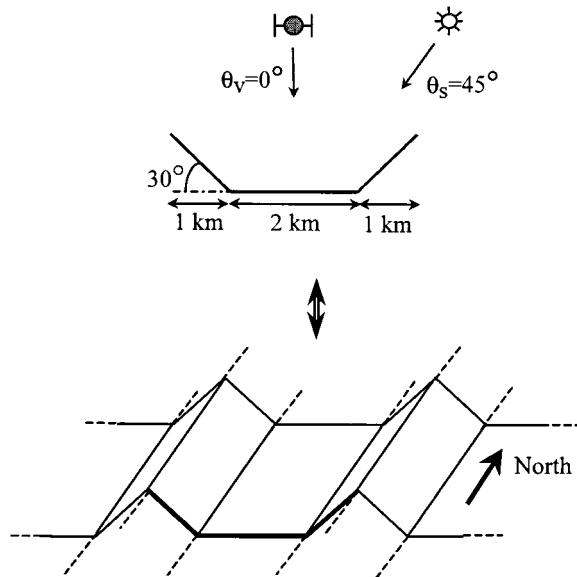


Fig. 7. Linear sand dunes.

shows the variation of the direct transmission with the altitude, as can be seen on the part of the curve that corresponds to the left side of the dune [0–1 km in Fig. 8(a)]. The diffuse sky radiances originate mainly from the aerosols, as their optical thickness in the present case is larger than the molecular optical thickness. The aerosol phase function is strongly forward scattering. Consequently, the left side of the dune receives more diffuse radiance than the

right side, consistent with the progressive decrease of the diffuse irradiance level with the slope. Note that using an isotropic model<sup>15,16</sup> for sky diffuse radiances would generate a symmetrical distribution of diffuse irradiance (because of the relief symmetry), whereas in this example there is almost a factor-of-2 difference between the values on the left and the right sides of the dune.

The contributions that come from reflections from neighboring areas are related to the direct and diffuse irradiance and to the geometry. Around slope transitions, the view factors of the neighboring pixels are larger (because of their closeness), so the adjacency terms reach their maximum at the slope transition level. The Earth–atmosphere coupling depends not only on the ground reflectance but also on the atmosphere’s properties (optical thickness, spherical albedo) and the terrain shape. Consequently it is the most difficult to interpret because it results from complex processes. The behavior of the Earth–atmosphere coupling term is slightly variable over this terrain. The presence of the dune, however, does play a significant role, as the mean value of this term in this case is ~20% greater than the same value computed on entirely flat ground. (This value was computed with the 6S code.) From these plots we can deduce that, on the left-hand side of the terrain profile, which is more exposed to the direct solar beam, the contributions of adjacency and environmental irradiance components do not exceed 10%. However, on the right-hand side of the dune, where the direct solar beam is small, the contribu-

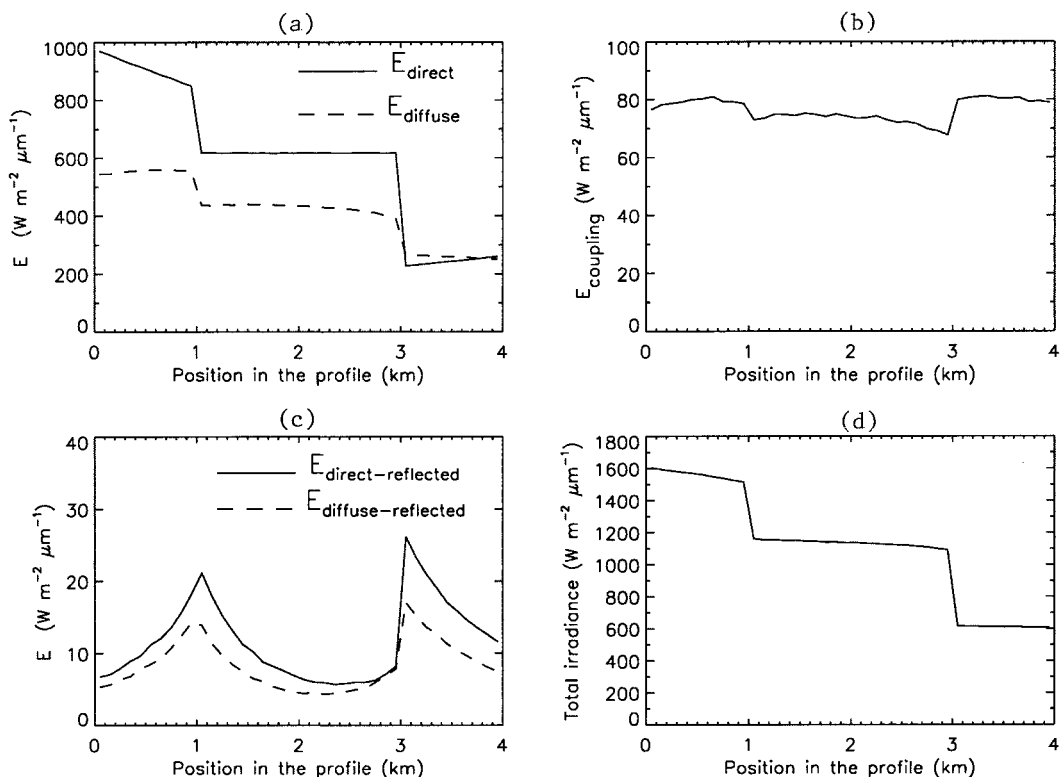


Fig. 8. Irradiance terms over linear sand dunes.

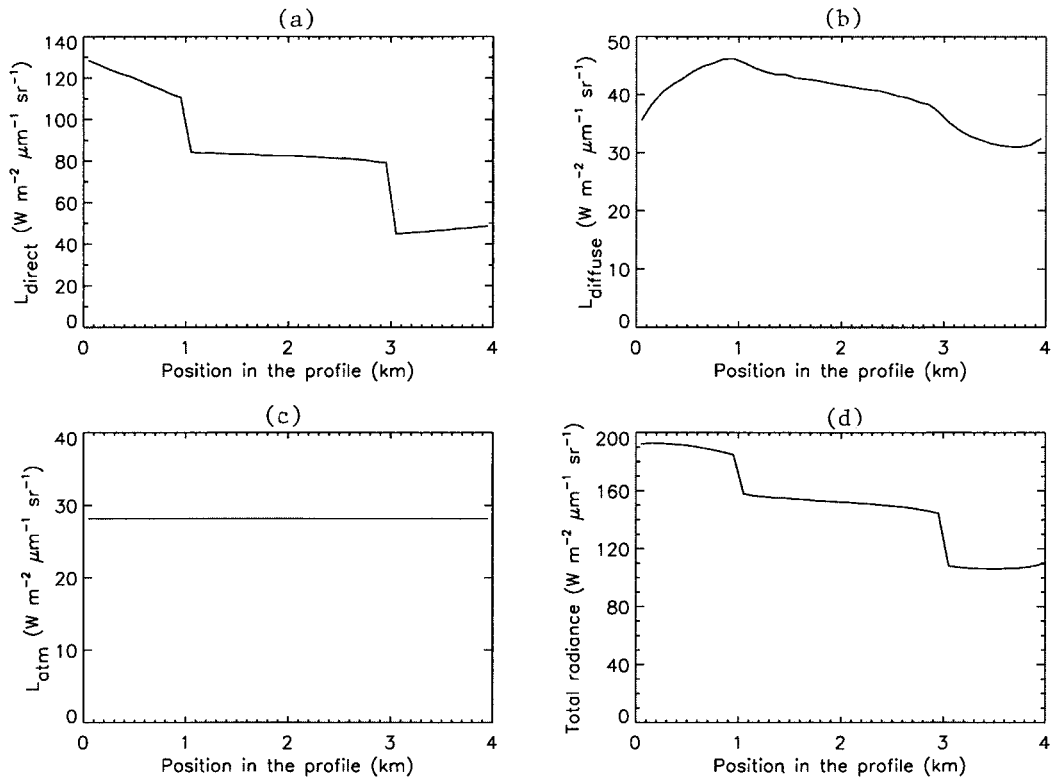


Fig. 9. Radiance terms observed over linear sand dunes.

tions of these components amount to more than 20% at the slope transition.

As the ground reflectance is Lambertian in this simulation, the direct radiance at satellite level [Fig. 9(a)] is directly related to the ground total irradiance

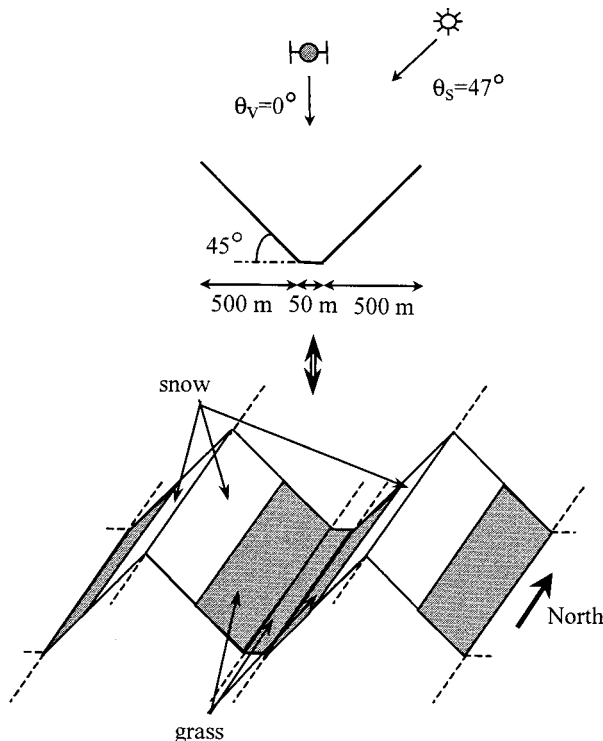


Fig. 10. Deep valley between snow-covered hilltops.

and to the direct upward path transmission, which varies with pixel altitude. The diffuse component [Fig. 9(b)] is smoother because it comes from atmospheric scattering events above the viewed pixel. The main effect of the relief on the shape of the total sensor radiance [Fig. 9(d)] is to produce three levels, each related to one of the distinct slopes that are present in the topography. The variations observed over this rugged ground amount to almost  $\pm 30\%$  of the mean value of the total radiance over the profile. The importance of the slope effect is thus not negligible. It can be seen as well that on the flat part of the profile between dunes the signal at sensor level is more than 10% greater than the signal that would be received over an entirely flat terrain. (This signal was again computed by the 6S code.) The main conclusion is that a hilly terrain induces effects that are linked not only to the local slope variations but also to environmental and adjacency effects.

### C. Shadow Effects on Highly Reflecting Ground

Now consider the more extreme configuration of a deep valley between snow-covered hills (Fig. 10). As Fig. 10 illustrates, the surface is snow covered for altitudes higher than 250 m, whereas the valley bottom up to 250 m is covered with short green grass. Because of the lack of available data for high zenith angles, we use simple reflectance models, which reproduce the bidirectional reflectance behavior of snow and short grass. These models are inspired by measurements presented in several studies<sup>17-19</sup> and consist of a diffuse (Lambertian) term added to a

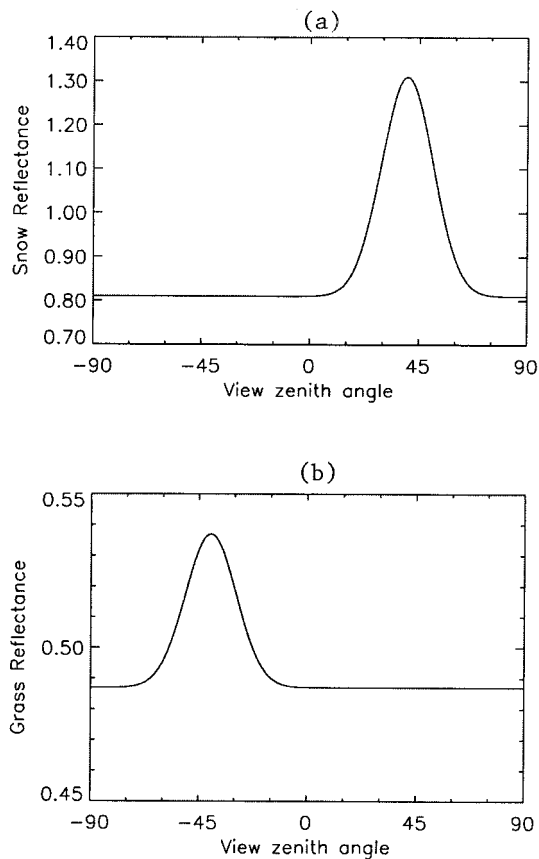


Fig. 11. Reflectance models of snow and grass. Negative values of zenith are used for backward scattering.

Gaussian term that corresponds to forward scattering for snow and backward scattering for grass. The spectral albedos at 850 nm of each surface type are chosen from the ASTER database<sup>12</sup> (0.85 for snow and 0.49 for grass). The reflectance values of the models in the principal plane for an incidence of 40° are illustrated in Fig. 11. The atmospheric model is kept unchanged from Subsection 2.B, and the aerosol visibility is set to 23 km. To create a shadowed area we set the solar zenith angle to 47°; the sensor is placed at satellite level and is nadir viewing.

The irradiance results of the Monte Carlo simulation at 850 nm are shown in Fig. 12. The direct component [Fig. 12(a)] depicts which part of the valley is shadowed. The diffuse component [Fig. 12(b)] is similar to that for the dune. However, because the atmosphere is cleaner, the overall values are smaller than in Fig. 8(b). The Earth-atmosphere coupling irradiance decrease in the valley bottom is predictable: The environmental component originates from the sky above, and, as pixels approach the valley floor, the solid angle of the sky decreases. The direct-reflected and diffuse-reflected components are particularly important on the side of the valley that does not receive direct solar irradiance. The fact that the direct-reflected term is nonzero on the left side of the valley might be surprising because there is no direct irradiance on the shadowed side. The received energy in this case comes from multiple reflections on the ground without any interaction with the atmosphere along the path. The direct-reflected signal coming from multiple reflections is generally neg-

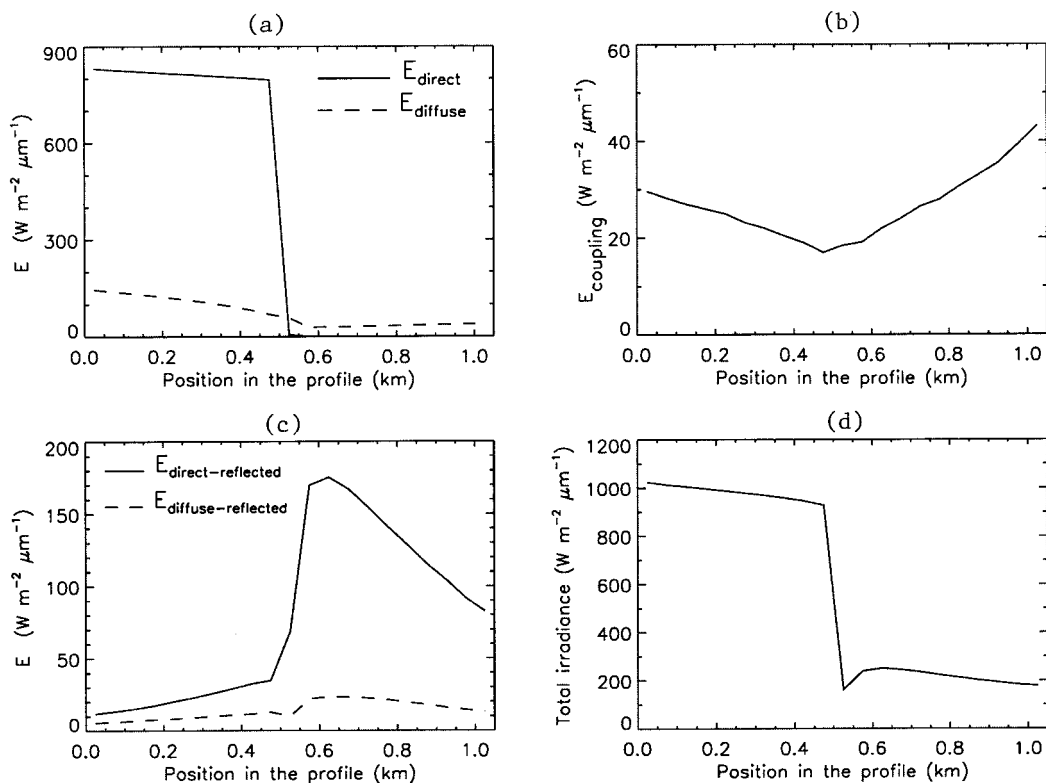


Fig. 12. Irradiance terms over the deep valley.

ligible, but in this simulation, because of the high reflectance values and the proximity of the sides of the valley, it reaches a significant level. Even though the direct and diffuse components have larger magnitudes on the left side of the valley (the first 0.25 km), the contribution to irradiance of the three environmental and adjacency terms (coupling, direct-reflected, diffuse-reflected) exceeds 6%. On the right side of the valley, which is not directly irradiated and receives little diffuse irradiance, the adjacency and environmental terms contribute the most to the total irradiance, reaching  $\sim 85\%$  on average over the entire right side. These environmental terms are consequently significant for analysis of satellite data over such a relief.

At satellite level, because the atmosphere is particularly clear, the direct radiance component dominates the total radiance [Fig. 13(a)]. The diffuse radiance does not vary significantly over the valley, as scattering by the atmosphere smooths the energy reflected by the surface. Therefore the diffuse radiance plays a role similar to that of the atmospheric intrinsic radiance by simply shifting the total radiance to a higher value.

#### 4. Conclusions

In this study a Monte Carlo method has been developed both to solve the radiative transfer equation and to simulate remote observations over rugged and heterogeneous scenes. This method permits the quantification of the Earth-atmosphere coupling irradiance at ground level, even for complex relief

and reflectance models. It also enables one to characterize the upward diffuse path over rugged terrain. The Monte Carlo method is subsequently used to simulate the surface irradiances and the top of atmosphere radiances over three complex surface scenes.

The first scene is a reflectance step at ground level, which we used to estimate the low-pass effects of the atmosphere. The second scene considered is a linear dunes desert landscape. The results for this simulation show that the presence of the relief may introduce a 10% error when the relief is neglected, even if the target is situated between the dunes in the flat part of the landscape, because of the adjacency and environmental terms introduced and modified by the relief. The last configuration presents an extreme case in which high-reflectance models and severe slopes are considered. In the shadowed area of this simulation, the irradiance components coming from reflections off neighboring regions dominate the total irradiance at ground level. These results indicate that the environmental and adjacency components have to be evaluated as soon as a relief with high reflectance values is present. These components may then play a significant, or even dominant, role in the signal measured by a satellite sensor over poorly exposed or shadowed areas.

The next step of our research effort will be to use the Monte Carlo method to interpret top-of-atmosphere satellite radiance measurements. In particular, we shall use this method to analyze the TOA bidirectional reflectance measured over a desert site in Algeria. The goal will be to explain the asym-

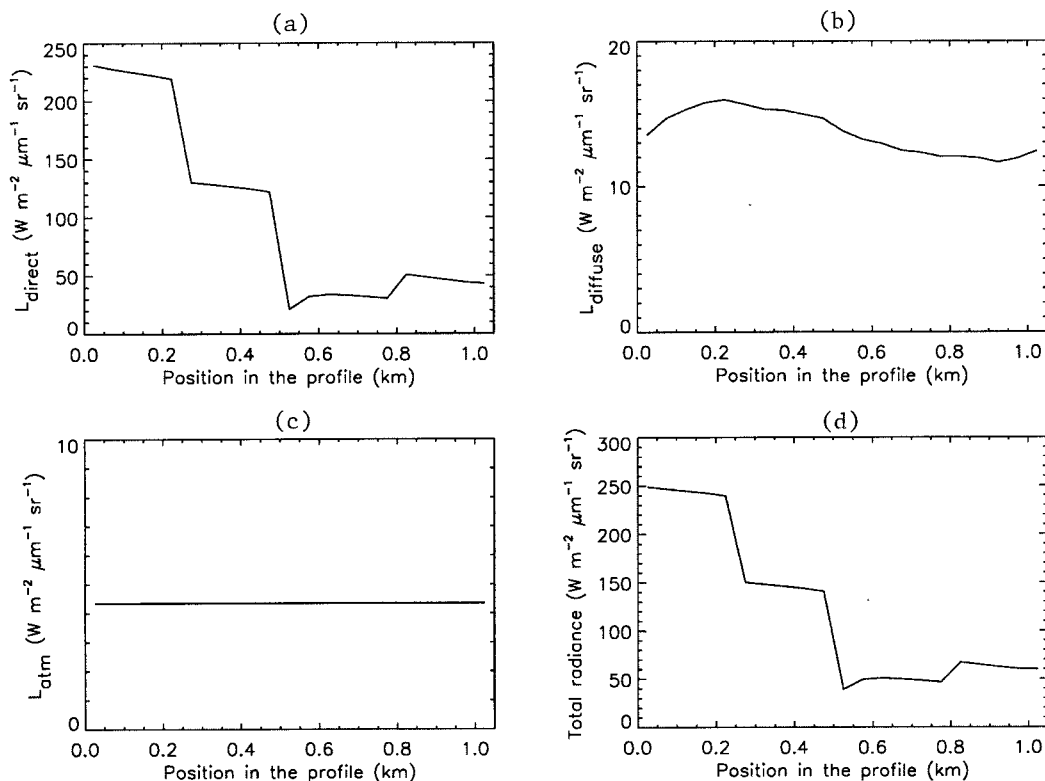


Fig. 13. Radiance components over the deep valley.

metry of the bidirectional reflectance with respect to the principal (solar) plane as observed by the POLDER (polarization and directionality of the Earth's reflectances) instrument.

## Appendix A

### 1. Free-Path Length

The probability of interaction of a photon with atmospheric particles between positions B and B + dB on a path starting from a point A is derived from

$$dL = -\sigma_e(B)L(B)dB, \quad (A1)$$

where  $L(B)$  is the transmitted radiance at position B and  $\sigma_e$  is the total extinction coefficient of the medium at B. This probability is then given by

$$dp(B, B + dB) = \exp\left[-\int_A^B \sigma_e(C)dC\right]\sigma_e(B)dB. \quad (A2)$$

The total extinction coefficient can be written as

$$\sigma_e(B) = \sigma_{s,mol}(B) + \sigma_{s,aero}(B) + \sigma_{a,mol}(B) + \sigma_{a,aero}(B), \quad (A3)$$

where the subscript  $s$  is associated with scattering,  $a$  with absorption,  $mol$  with molecules, and  $aero$  with aerosols. This expression gives the relative probabilities for the possible types of interaction that happen in the interval dB.

### 2. Scattering by Particles

In the case of scattering, the photon propagation direction is altered. The phase function that characterizes a given type of particle gives the spatial distribution of the scattered photons. In our model it is symmetric about the incidence direction, which is a reasonable assumption for spherical particles and randomly oriented nonspherical particles. Therefore we can write the phase function as  $p(\xi)$ , where  $\xi$  is the angle between the incident direction and the scattering direction. The function  $[p(\xi)/4\pi]d\omega$  represents the probability for a scattered photon to set off inside the solid angle  $d\omega = \sin(\xi)d\xi d\varphi$  centered on the direction  $(\xi, \varphi)$ , where  $\varphi$  is the scattering local azimuth angle.

For molecules, the Rayleigh phase function, i.e.,

$$p_{mol}(\xi) = (3/4)(1 + \cos^2 \xi), \quad (A4)$$

is used for  $p(\xi)$ , whereas for aerosols we use the Henyey–Greenstein expression<sup>10</sup>:

$$p_{aero}(\xi) = \frac{1 - g_\lambda^2}{(1 + g_\lambda^2 - 2g_\lambda \cos \xi)^{3/2}}, \quad (A5)$$

where  $g_\lambda$  is the asymmetry factor of the aerosols, which depends on the wavelength of the radiation and the compositions, sizes, and shapes of the aerosol particles.

### 3. Reflection at the Surface

A photon reaching the ground is absorbed or reflected according to the bidirectional reflectance of the surface  $\rho(\theta_s, \phi_s, \theta, \phi)$  (which corresponds to the definition of the bidirectional reflectance distribution function of Nicodemus<sup>20</sup> multiplied by  $\pi$ ). The probability of reflection  $\rho_p(\theta_s, \phi_s)$  can be written as<sup>21</sup>

$$\rho_p(\theta_s, \phi_s) = \int_{\phi=0}^{2\pi} \int_{\theta=0}^{\pi/2} \frac{\rho(\theta_s, \phi_s, \theta, \phi)}{\pi} \cos(\theta)\sin(\theta)d\theta d\phi, \quad (A6)$$

where  $\theta_s$  and  $\phi_s$  are the incident zenith and azimuth angles, respectively. The quantity  $\rho_p(\theta_s, \phi_s)$  corresponds to the spectral plane albedo. Provided that the complete bidirectional reflectance is known, i.e., over the whole hemisphere, the method can deal with complex reflectance models.

### 4. Simulation Process: Quantities of Interest

The Monte Carlo simulation consists in launching photons from the TOA as if they came from the Sun. Each photon is tracked through a sequence of interactions until it is absorbed in the atmosphere, observed at the surface, or scattered out of the atmosphere. Photons are accumulated on each pixel of the ground and each pixel of the sensor. After sufficiently many photons are processed, the irradiance and radiance values are deduced. Let us assume that we launched  $N$  photons across the horizontal surface area  $S_{TOA}$  at the TOA. If  $n_M$  photons were received on pixel  $M$  at ground level, the irradiance on  $M$  is given by

$$E(P) = \frac{n_M}{S_M} \frac{S_{TOA}}{N} E_{TOA} \cos \theta_s, \quad (A7)$$

where  $S_M$  is the surface area of pixel  $M$ ,  $E_{TOA}$  is the solar irradiance at the TOA, and  $\theta_s$  is the solar zenith angle. We make the distinction among the components illustrated in Figs. 1 and 2 during the simulation process by accumulating photons according to their respective histories. This expression is then valid for each irradiance type. At sensor level, each pixel  $m$  is associated with a receiving surface  $s_m$  and a viewing solid angle  $\Delta\omega_m$ . Using the number of photons  $n_m$  that reach this surface inside solid angle  $\Delta\omega_m$ , we calculate the corresponding radiance from

$$L(m) = \frac{n_m}{s_m \Delta\omega_m} \frac{S_{TOA}}{N} E_{TOA} \cos \theta_s. \quad (A8)$$

As before, the components are identified during the simulation process.

## References

1. B. N. Holben and C. O. Justice, "The topographic effect on spectral response from nadir-pointing sensors," *Photogramm. Eng. Remote Sens.* **46**, 1191–1200 (1980).
2. D. S. Kimes and J. A. Kirchner, "Modeling the effects of various radiant transfers in mountainous terrain on sensor response," *IEEE Trans. Geosci. Remote Sens.* **GE-19**, 100–108 (1981).
3. T. Kusaka, Y. Kawata, S. Ueno, and S. Furumoto, "Removal of

- the atmospheric and topographic effects from the rugged terrain image data remotely sensed by Landsat," in *Proceedings of International Geoscience and Remote Sensing Symposium* (Institute of Electrical and Electronic Engineers, Piscataway, N.J., 1987), Vol. 1, pp. 649–652.
4. T. Kusaka, Y. Kawata, H. Egawa, and S. Ueno, "Signature variations due to atmospheric and topographic effects on satellite MSS data over rugged terrain," in *Proceedings of International Geoscience and Remote Sensing Symposium* (European Space Agency, Paris, 1988), pp. 825–828.
  5. T. Kusaka and Y. Kawata, "Atmospheric and topographic correction of satellite data over mountainous terrain," in *Proceedings of International Geoscience and Remote Sensing Symposium* (Institute of Electrical and Electronics Engineers, Piscataway, N.J., 1994), Vol. 1, pp. 58–60.
  6. R. Richter, "Correction of atmospheric and topographic effects for high spatial resolution satellite imagery," *Intl. Remote Sens.* **18**, 1099–1111 (1997).
  7. C. Proy, D. Tanré, and P. Y. Deschamps, "Evaluation of topographic effects on remotely sensed data," *Remote Sens. Environ.* **30**, 21–32 (1989).
  8. E. Vermote, D. Tanré, J. L. Deuzé, M. Herman, and J. J. Morcrette, "Second simulation of the satellite signal in the solar spectrum, 6S: an overview," *IEEE Trans. Geosci. Remote Sens.* **35**, 675–686 (1997).
  9. G. I. Marchuk, G. A. Mikhailov, M. A. Nazaraev, R. A. Dabinjan, B. A. Kargin, and B. S. Elepov, *The Monte Carlo Methods in Atmospheric Optics*, D. L. MacAdam, ed., Vol. 12 of Springer Series in Optical Sciences (Springer-Verlag, Berlin, 1980), pp. 5–17.
  10. J. Lenoble, *Atmospheric Radiative Transfer* (Deepak, Hampton, Va., 1993).
  11. R. McClatchey, R. W. Fenn, J. E. A. Selby, F. E. Volz, and J. S. Garing, "Optical properties of the atmosphere," Report 71.0279, Environmental Research Paper 354 (U.S. Air Force Cambridge Research Laboratory, Bedford, Mass., 1971).
  12. ASTER (Advanced Spaceborne Thermal Emission and Reflection Radiometer) spectral library, NASA: <http://speclib.jpl.nasa.gov/>; cognizant scientist, [simon.j.hook@jpl.nasa.gov](mailto:simon.j.hook@jpl.nasa.gov).
  13. Y. J. Kaufman, "Atmospheric effect on spatial resolution of surface imagery: errata," *Appl. Opt.* **23**, 4164–4172 (1987).
  14. H. Cosnefroy, M. Leroy, and X. Briottet, "Selection and characterization of Saharan and Arabian desert sites for the calibration of optical satellite sensors," *Remote Sens. Environ.* **58**, 101–114 (1996).
  15. J. Dozier and J. Frew, "Atmospheric corrections to satellite radiometric data over rugged terrain," *Remote Sens. Environ.* **11**, 191–205 (1981).
  16. R. W. Sloberg and B. K. P. Horn, "Atmospheric effects in satellite imaging of mountainous terrain," *Appl. Opt.* **22**, 1703–1716 (1983).
  17. J. Dozier, R. E. Davis, A. T. C. Chang, and K. Brown, "The spectral bidirectional reflectance of snow," in *Proceedings of the 4th International Colloquium on Spectral Signatures of Objects in Remote Sensing* (European Space Agency, Paris, 1988), pp. 87–92.
  18. S. G. Warren, "Optical properties of snow," *Rev. Geophys. Space Phys.* **20**, 67–89 (1982).
  19. M. M. Verstraete, B. Pinty, and R. E. Dickinson, "A physical model of the bidirectional reflectance of vegetation canopies. 2. Inversion and validation," *J. Geophys. Res.* **95**, 11,767–11,775 (1990).
  20. F. E. Nicodemus, "Reflectance nomenclature and directional reflectance and emissivity," *Appl. Opt.* **9**, 1474–1475 (1970).
  21. Y. M. Govaerts and M. M. Verstraete, "Raytran: a Monte Carlo ray-tracing model to compute light scattering in three-dimensional heterogeneous media," *IEEE Trans. Geosci. Remote Sens.* **36**, 493–504 (1998).